

# RSC Advances



This is an *Accepted Manuscript*, which has been through the Royal Society of Chemistry peer review process and has been accepted for publication.

*Accepted Manuscripts* are published online shortly after acceptance, before technical editing, formatting and proof reading. Using this free service, authors can make their results available to the community, in citable form, before we publish the edited article. This *Accepted Manuscript* will be replaced by the edited, formatted and paginated article as soon as this is available.

You can find more information about *Accepted Manuscripts* in the [Information for Authors](#).

Please note that technical editing may introduce minor changes to the text and/or graphics, which may alter content. The journal's standard [Terms & Conditions](#) and the [Ethical guidelines](#) still apply. In no event shall the Royal Society of Chemistry be held responsible for any errors or omissions in this *Accepted Manuscript* or any consequences arising from the use of any information it contains.

# Sol-gel synthesis of Ni and Ni supported catalysts for hydrogen production by methane decomposition

Yi Shen<sup>\*a, b</sup> and Aik Chong Lua<sup>\*b</sup>

<sup>a</sup> College of Light Industry and Food Sciences, South China University of Technology, Guangzhou, 510640, P. R. China, Tel. & Fax: +86 2087113843; email: feyshen@scut.edu.cn

<sup>b</sup> School of Mechanical and Aerospace Engineering, Nanyang Technological University, 50 Nanyang Avenue, 639798, Republic of Singapore, Tel.: +65 67905535, email: maclua@ntu.edu.sg

## Abstract

NiO and NiO-CuO, NiO-TiO<sub>2</sub> and NiO-CeO<sub>2</sub> were synthesized by the sol-gel method and these metal oxides were further processed into catalysts for hydrogen production by thermocatalytic decomposition of methane. The structures of the metal oxides and catalysts were extensively characterized by transmission electron microscopy, X-ray diffraction, energy dispersive X-ray spectroscopy, X-ray photoelectron spectroscopy, temperature-programmed reduction and N<sub>2</sub> adsorption. The catalytic performance of the catalysts was evaluated in terms of methane conversion and carbon yield. NiO had a BET surface area of 66 m<sup>2</sup>/g. When compared with NiO, NiO-CuO had a lower BET surface area of 13 m<sup>2</sup>/g while NiO-TiO<sub>2</sub> and NiO-CeO<sub>2</sub> had higher BET surface areas of 161 and 133 m<sup>2</sup>/g, respectively. The resulting supported catalysts required increased reduction temperature and had higher Ni 2p<sub>3/2</sub> binding energy, indicating strong metal-support interactions. For the Ni-Cu catalyst, the introduction of copper resulted in a lower Ni 2p<sub>3/2</sub> binding energy due to the charge transfer from Cu to the adjacent Ni atoms. The Ni catalyst showed a stable methane conversion of 0.39 at 550°C. The presence of copper in the Ni-Cu catalyst increased the working temperature but decreased methane conversion. The Ni-TiO<sub>2</sub> and Ni-CeO<sub>2</sub> catalysts exhibited stable methane conversions of 0.56 and 0.60, respectively at 575°C. The lifetime tests of the catalysts revealed that the Ni catalyst had a life span of 600 min at 550°C, resulting in a carbon yield of 121 g C/g Ni. The Ni-Cu, Ni-CeO<sub>2</sub> and Ni-TiO<sub>2</sub> catalysts had life spans of 670, 790 and 840 min at 575°C, resulting in carbon yields of 171, 204 and 256 g C/g Ni, respectively. The structures of the resulting carbon products were characterized by transmission electron microscopy and X-ray diffraction. It was found that the morphology of the resulting carbon was dependent on the type of catalyst used.

## 1. INTRODUCTION

It is established that global warming is taking place due to human activities, in particular, the combustion of fossil fuels. Due to its immense negative impacts on human communities and ecosystems, global warming has been the most dangerous environmental problem of the contemporary world and has attracted great attention from the scientific and political communities. To address this urgent problem, the key point is to control the emissions of greenhouse gases and develop renewable energy sources. Hydrogen is considered to be one of the most efficient and environmentally friendly energy carriers and considerable research has been carried out into eco-friendly methods of hydrogen production.<sup>1, 2</sup> For decades, steam reforming of natural gas using nickel as catalyst has been the most widely used process for the industrial production of hydrogen. However, the production of hydrogen by this multistep process results in high emissions of carbon dioxide and the end-product always contains some quantities of carbon monoxide, which prevents the resulting hydrogen being directly used in fuel cells. Alternatively, thermocatalytic decomposition of methane (TDM) has been of great interest because only pure hydrogen and high quality carbon are obtained in this process.<sup>3-6</sup> CO<sub>x</sub>-free hydrogen produced by TDM is favourable for fuel cell applications without further separation and purification processes. In addition, carbon is sequestered in the form of valuable solid carbon nanotubes or nanofibers rather than as a notorious greenhouse gas in the form of carbon dioxide. The feasibility of TDM process is highly dependent on the efficiency and durability of the catalyst. Nickel has been the most efficient catalyst and extensively studied for the TDM process.<sup>7-10</sup> Considerable work has focused on the catalyst preparation and the selection of catalyst support. Impregnation,<sup>11-15</sup> co-precipitation<sup>16-22</sup> and fusion method<sup>23-26</sup> have been widely used to prepare active catalysts. Sol-gel technique is a well-established method to prepare various catalysts with high porosities and uniform dispersions of active components on supports.<sup>27, 28</sup> However, limited work was reported on the syntheses of catalysts by the sol-gel method for TDM process.<sup>29</sup> It was reported that the supported catalysts obtained by the sol-gel technique exhibited strong metal-support interactions, which could stabilize the active component at high reaction temperatures.<sup>30</sup> In this work, nickel oxide and nickel oxide supported on copper oxide, titanium oxide and cerium oxide were synthesized by the sol-gel method using a nontoxic and biodegradable ethoxylated sorbitan ester as the structure-directing agent. After calcination and reduction, the resulting active nickel particles and supported nickel particles were investigated as

catalysts for the TDM process. The structures and catalytic performance of the resulting catalysts were fully characterized. The effects of copper promoter and supports on the catalytic activities of the catalysts were investigated.

## 2. EXPERIMENTAL SECTIONS

**2.1 Chemicals.** For the synthesis of the catalysts, the following chemicals were used: precursors - nickel (II) nitrate hexahydrate, copper (II) nitrate trihydrate, cerium (III) nitrate hexahydrate, and titanium (IV) butoxide ( $\text{Ti}(\text{OBU})_4$ ); acids - hydrochloric acid (HCl) and acetate acid; surfactant - ethoxylated sorbitan ester, namely, Tween 20; and solvent – ethanol. These chemicals were used as received.

**2.2 Synthesis of NiO and NiO on metal oxide supports.** Nickel oxide and nickel oxide on metal oxide supports were synthesized using a similar sol-gel method reported by Fan *et al.*<sup>31</sup> In a typical nickel oxide synthesis process, 4 ml of Tween 20, 40 mmol of acetate acid, 24 mmol of HCl and 30 mmol of nickel (II) nitrate hexahydrate were dissolved in 60 ml of ethanol. The mixture was stirred vigorously for 2 h at room temperature and then aged at 60°C in an oven for 2 days. After the complete evaporation of ethanol, the as-synthesized composite was calcined at 500°C in air for 5 h. For the synthesis of supported nickel oxides, nickel (II) nitrate hexahydrate and the other metal salt with a mole ratio of 1:1 were used as precursors. For instance, in the synthesis of nickel oxide supported on titanium oxide, 4 ml of Tween 20, 40 mmol of acetate acid, 24 mmol of HCl, 15 mmol of nickel (II) nitrate hexahydrate and 15 mmol of  $\text{Ti}(\text{OBU})_4$  were dissolved in 60 ml of ethanol. The synthesis procedures were identical to those of the nickel oxide. For convenience, the nickel oxide, nickel oxide supported on copper oxide, nickel oxide supported on titanium oxide and nickel oxide supported on cerium oxide were denoted as NiO, NiO-CuO, NiO-TiO<sub>2</sub> and NiO-CeO<sub>2</sub>, respectively.

**2.3 Temperature-programmed reduction of nickel oxide.** The temperature-programmed reduction (TPR) of nickel oxide was carried out using an experimental set-up equipped with a temperature-programmed controller, similar to that described by Liotta *et al.*<sup>32</sup> In a typical process, 0.25 g of metal oxide was loaded into a quartz tube reactor. A mixture of hydrogen and nitrogen with a volume ratio of 1:3 was introduced as the reducing agent with a flowrate of 20 ml/min. The temperature of the reactor was increased at a rate of 2.5°C/min. The composition of

the gas stream was continuously analyzed. NiO, NiO-CuO, NiO-TiO<sub>2</sub> and NiO-CeO<sub>2</sub> were reduced to Ni, NiCu, Ni-TiO<sub>2</sub> and Ni-CeO<sub>2</sub>, respectively.

**2.4 Catalyst characterization.** A field emission scanning electron microscope (FESEM) (JSM-7600F, JEOL) and a transmission electron microscope (JSM2010, JEOL) were used to observe the morphology of the catalysts and the resulting carbon materials. To analyze the crystalline structures of the catalysts and the resulting carbon materials, X-ray diffraction (XRD) patterns were obtained by a diffractometer (PW1830, Philips) equipped with Cu-K $\alpha$  radiation of 1.54 Å. The N<sub>2</sub> adsorption-desorption isotherms were obtained using the accelerated and surface area porosimetry system (ASAP 2010, Micromeritics). The pore surface area was calculated using the Brunauer-Emmett-Teller (BET) method; the pore volume and pore size were calculated by the Barret-Joyner-Halenda (BJH) method. An energy dispersive X-ray (EDX) analyzer and an X-ray photoelectron spectroscopy (XPS) were used to analyze the elemental composition and binding energy of the samples, respectively. To characterize the reactive catalysts after hydrogen reduction, a passivation treatment was conducted. After the nickel oxide was reduced in the quartz tube, it was subsequently cooled down to ambient temperature in a nitrogen atmosphere. Then, an O<sub>2</sub>/N<sub>2</sub> (0.5%:99.5%) mixture stream was introduced to the catalysts for 4 h at room temperature before the sample was removed from the reactor.

**2.5 Catalytic activity characterization.** The catalytic activities of the catalysts were tested by an experimental set-up.<sup>33, 34</sup> In a typical process, a predetermined amount of catalyst was loaded into the mid-section of a quartz tube reactor, having an internal diameter of 10 mm and a length of 800 mm. The reactor was surrounded and heated by an electric furnace (Lenton) with a temperature programmed controller (Carbonite 2416) and the temperature of the reactor was accurately monitored using a K-type thermocouple. The flow rates of the gases were measured and controlled by mass flowmeters (Alicat Scientific). Prior to the catalytic reaction, the system was flushed with nitrogen to remove the air. The concentrations of the gases at the reactor outlet were analysed by a calibrated gas chromatograph (Agilent 6890-5973 GC-MS network systems) equipped with a thermal conductivity detector.

### 3. RESULTS AND DISCUSSION

**3.1 Structures of the catalysts.** The elemental composition of the as-synthesized metal oxides was determined from the EDX tests and the results are shown in Table 1. It was found that all the

fresh metal oxides contained a small quantity of chlorine element, *e.g.*, the fresh NiO-CeO<sub>2</sub> sample consisted of 9 mmol.% chlorine atom as shown in Table 1 and Figure 1. The existence of chlorine atoms in the fresh metal oxides in the form of NiCl<sub>2</sub> (as confirmed by the XRD tests but not shown here) was due to the incomplete hydrolysis of Ni<sup>2+</sup> during the sol-gel process. This phenomenon was also reported by Fan *et al.*<sup>31</sup> The presence of NiCl<sub>2</sub> as an impurity in the fresh metal oxides was detrimental to the subsequent catalytic activity in the TDM process. Hence, NiCl<sub>2</sub> was removed by thoroughly washing the as-synthesized metal oxides using DI water and the end results were evidenced from the EDX results in Table 1 and Figure 1. After the wash, the NiO content was determined to be 40.5, 15.3 and 43.8% in the NiO-TiO<sub>2</sub>, NiO-CeO<sub>2</sub> and NiO-CuO catalyst, respectively. The nitrogen adsorption-desorption isotherms of the metal oxides are shown in Figure 2. The BET surface area and pore size are shown in Table 1. NiO had a BET surface area of 66 m<sup>2</sup>/g. When compared with NiO, NiO-CuO had a lower BET surface area of 13 m<sup>2</sup>/g while NiO-TiO<sub>2</sub> and NiO-CeO<sub>2</sub> had higher BET surface areas of 161 and 133 m<sup>2</sup>/g, respectively.

Figure 3 shows the TEM micrographs of the metal oxides. The NiO particles showed cuboid-like morphology with lengths of 50-120 nm as shown in Figure 3A. A closer examination revealed that the surface of the NiO particle was rough and some worm-like pores of 1-2 nm were observed (inset in Figure 3A). The formation of these worm-like pores was attributed to the supermolecular templating of Tween 20 surfactant. The NiO-CuO particles exhibited irregular-spherical structures with varying diameters from 40 to 100 nm. Some worm-like pores were also observed in the particles. In contrast, NiO-CeO<sub>2</sub> and NiO-TiO<sub>2</sub> had average particle sizes of 11 and 9 nm, respectively, which were much smaller than those of NiO and NiO-CuO, indicating that the presence of Ce<sup>4+</sup> and Ti<sup>4+</sup> had significant effects on the hydrolysis of Ni<sup>2+</sup> during the sol-gel process. The hydrolysis constants ( $K_a$ s) of metal ions are highly dependent on the ionic charge and radius. The  $pK_a$  values follow the order of Ni<sup>2+</sup> (9.9) > Cu<sup>2+</sup> (7.9) > Ce<sup>4+</sup> (-1.1) > Ti<sup>4+</sup> (-4.0).<sup>35</sup> Therefore, the hydrolysis of Ni<sup>2+</sup> could be overwhelmed by those of Ce<sup>4+</sup> and Ti<sup>4+</sup> during the sol-gel process. In this study, the inhibition on the hydrolysis of Ni<sup>2+</sup> could be further intensified due to the scarcity of water which was exclusively originated from the reaction of ethanol and acetate acid during the sol-gel process. No distinct pores were observed on the surfaces of NiO-CeO<sub>2</sub> and NiO-TiO<sub>2</sub> particles, indicating the failure of the templating effect of

the surfactant. This could probably be related to the branched structure of Tween 20 and the kinetics of the sol-gel process.

Figure 4 shows the XRD patterns of the metal oxides. The XRD pattern of NiO showed diffraction peaks at 37.3, 43.3, 62.9 75.4 and 79.4°, which could be assigned to the rhombohedral phase of NiO (JCPDS #44-1159). For NiO-CuO, separate NiO and CuO diffractions were observed, indicating that NiO and CuO did not form solid solution during the sol-gel process. The peaks in the XRD patterns for NiO-CeO<sub>2</sub> and NiO-TiO<sub>2</sub> could be ascribed to the diffractions of NiO and the supports (CeO<sub>2</sub> JCPDS: #1-0800; TiO<sub>2</sub> JCPDS: #1-0562). The crystal sizes of NiO in the metal oxides were calculated from the strongest (012) diffraction peaks and these sizes are given in Table 2. No other phases were identified in the XRD patterns, confirming that the metal oxides were free of impurities after the thorough wash.

Figure 5 shows the hydrogen uptake of the metal oxides as a function of temperature. NiO showed a reduction peak at approximately 377°C as it commenced to be reduced at about 350-450°C. NiO-CuO metal oxides exhibited two distinguishable reduction peaks centred at about 235 and 345°C, which corresponded to the reduction of Cu<sup>2+</sup> and Ni<sup>2+</sup>, respectively. The Cu<sup>2+</sup> can be reduced at lower temperatures because it has a higher standard reduction potential (Cu<sup>2+</sup>→Cu<sup>0</sup> +0.34V) than that of Ni<sup>2+</sup> (Ni<sup>2+</sup>→Ni<sup>0</sup> -0.26V). It had been reported that the presence of metallic Cu could enhance the reducibility of the Ni species due to the fact that metallic copper could dissociate the hydrogen molecule into hydrogen atoms which could be spilled over to the surface of the neighbouring NiO. This led to a lower NiO reduction temperature in the NiO-CuO metal oxides when compared with that of NiO.<sup>34</sup> The NiO-TiO<sub>2</sub> metal oxides showed a broad reduction peak centred at 409°C, which was attributed to the reduction of Ni species. A closer inspection on the TPR curve showed that this broad peak had a shoulder at lower temperatures and a long tail at higher temperatures. It was suggested that supported catalysts, such as Ni/Al<sub>2</sub>O<sub>3</sub> and Ni/MgO, had higher reduction temperatures due to the interactions between NiO and the support.<sup>36</sup> Correspondingly, for the TPR curve of NiO-TiO<sub>2</sub>, the shoulder at lower temperatures could be ascribed to the reduction of the surface NiO particles that had weak binding to the TiO<sub>2</sub> while the long tail at higher temperatures was related to the reduction of Ni<sup>2+</sup> which was strongly attached to TiO<sub>2</sub>. The TPR pattern of NiO-CeO<sub>2</sub> showed continuous hydrogen consumption at around 350-600°C. The consumption of hydrogen at lower temperatures (approximately less than 500°C) could be ascribed to the reduction of Ni<sup>2+</sup> while

the consumption of hydrogen at higher temperatures could be due to the reduction of  $Ce^{4+}$ .<sup>37</sup> It should be noted that the reduction temperature is also highly dependent on the particle size, *i.e.*, smaller particle sizes result in lower reduction temperatures. Considering the small particle sizes of NiO in the NiO-TiO<sub>2</sub> and NiO-CeO<sub>2</sub> metal oxides, the NiO-TiO<sub>2</sub> and NiO-CeO<sub>2</sub> metal oxides obtained using the sol-gel method in this study had reasonable high reduction temperatures, indicating the strong interactions between the NiO and the supports.

Figure 6 shows TEM micrographs of the catalysts after hydrogen reduction. After reduction, the resulting metallic Ni particles had smaller particle sizes of 30-90 nm as compared with the NiO particles. The Ni particles remained as mono-dispersed without sintering as shown in Figure 6A. The reduced Ni-Cu alloy particles, on the contrary, had larger particle sizes as shown in Fig. 6(B) when compared with the pristine NiO-CuO particles in Fig. 3(B). The enlarged Ni-Cu alloy particles could be due to the amalgamation of NiO and CuO particles during hydrogen reduction. The reduced Ni-CeO<sub>2</sub> and Ni-TiO<sub>2</sub> catalyst particles in Fig. 6 (C) and (D) exhibited similar morphology with average diameters of 11 and 9 nm, respectively, which were of similar sizes to those of NiO-CeO<sub>2</sub> and NiO-TiO<sub>2</sub> metal oxide particles in Fig. 3(C) and (D), respectively.

Figure 7 shows the XRD patterns of the catalysts after hydrogen reduction. The NiO metal oxide after reduction shows three prominent peak diffractions at 44.5, 51.9 and 76.5°, which can be ascribed to the metallic Ni planes (111), (200) and (220), respectively (JCPDS #4-0850). The  $d_{(111)}$  spacing value and lattice parameter of Ni were calculated to be 2.04 and 3.53 Å, respectively, based on the Ni (111) diffraction. For the NiO-CuO metal oxide, Ni-Cu alloy was formed after hydrogen reduction as indicated by the symmetric peaks centred at 43.9, 51.1 and 75.2°. The  $d_{(111)}$  spacing value and lattice parameter of the Ni-Cu alloy were determined and found to be 2.07 and 3.58 Å, respectively, which were almost equal to the theoretical values of 2.06 and 3.57 Å as obtained by Vegard's law. The metallic Ni diffractions can be identified in the XRD patterns of the Ni-TiO<sub>2</sub> and Ni-CeO<sub>2</sub> catalysts although the intensity of the diffractions decreased significantly due to the decrease in Ni content in the supported catalysts. The crystal sizes of Ni in the metal oxides and catalysts were also calculated and shown in Table 2.

Figure 8 shows the evolution of the Ni  $2p_{3/2}$  core level spectra of the catalysts after hydrogen reduction and the results of the XPS analysis are summarized in Table 2. All the spectra were corrected using the C 1s signal located at 284.5 eV. The Ni  $2p_{3/2}$  spectrum exhibits a main peak

located at 851-858 eV and a satellite peak at higher binding energy (BE) of 861.3-862.1 eV, which could be attributed to  $2p^53d^0L$  and  $2p^53d^8L$  (L means a ligand hole) final states, respectively.<sup>38</sup> To decompose the spectra, the constraints of equal spin-orbit splitting for Ni  $2p_{3/2}$  peaks in BE, peak area and full width at half maximum were thoroughly considered. The deconvolution of the Ni  $2p_{3/2}$  main peak yielded three peaks at 851.6-852.8, 854.3-855.6, and 856.5-857.8 eV, which could be assigned to Ni<sup>0</sup>, Ni<sup>2+</sup> and Ni<sup>3+</sup>, respectively. The identification of the third peak at 856.5-857.8 eV is controversial since Ni<sup>3+</sup> and Ni<sup>2+</sup> in solid solution have similar binding energies (BEs) in this range.<sup>38</sup> The variations of the third peak were also very complicated. The Ni-Cu alloy catalyst and Ni-CeO<sub>2</sub> catalyst had higher BEs while the Ni-TiO<sub>2</sub> catalyst had a lower BE of the third peak when compared with that of the Ni catalyst. Careful examination of the BEs of the Ni species indicated that when compared with the Ni catalyst, the Ni-TiO<sub>2</sub> and Ni-CeO<sub>2</sub> catalysts showed higher BEs of Ni<sup>0</sup> (+0.6 and +0.7 eV, respectively) and Ni<sup>2+</sup> (+0.5 and +0.7 eV, respectively) while the Ni-Cu alloy catalyst exhibited lower BEs of Ni<sup>0</sup> (-0.5 eV) and Ni<sup>2+</sup> (-0.6 eV) as shown in Table 2. The positive chemical shift of BEs observed on the Ni-TiO<sub>2</sub> and Ni-CeO<sub>2</sub> catalysts could be attributed to the electron transfer from the highly dispersed nickel to the support due to the Ni-support interactions.<sup>37</sup> This is consistent with the TPR results that the Ni-TiO<sub>2</sub> and Ni-CeO<sub>2</sub> catalysts had higher reduction temperatures. The decrease in the BEs of Ni<sup>0</sup> and Ni<sup>2+</sup> observed on the Ni-Cu alloy catalyst could probably be related to the changes in the electron density of nickel unfilled d-band due to the charge transfer from the relatively electropositive Cu (electronegativity 1.90) to the adjacent Ni (electronegativity 1.91) atoms.<sup>39</sup>

**3.2 Catalytic activities.** Figure 9 shows the conversion of methane over the catalysts using a stepwise heating mode and the methane conversion value at each temperature increment and dwell are given in Table 3. The Ni catalyst had stable methane conversion values of 0.25 and 0.29, at 500 and 550°C, respectively. The methane conversion increased to 0.46 at 575°C, but thereafter decreased sharply with increasing reaction time as shown in Figure 9. The increase in methane conversion with increasing reaction temperature is attributed to the endothermic nature of the reaction. The deactivation of Ni catalyst at 575°C could be due to the encapsulation of Ni particles by the deposited graphitic layers as reported by Wang and Lua.<sup>40</sup> The Ni-TiO<sub>2</sub> catalyst exhibited stable methane conversion values of 0.28 and 0.47 while the Ni-CeO<sub>2</sub> catalyst had stable methane conversion values of 0.30 and 0.47 at 500 and 550°C, respectively. These values

were higher than those of the Ni catalyst. This was attributed to the uniform dispersion of the fine Ni particles on the supports as indicated by the TEM micrographs (Figure 6C and 6D), which resulted in abundant active sites and fast accessibility for the methane molecules. The Ni-TiO<sub>2</sub> and Ni-CeO<sub>2</sub> catalysts achieved stable methane conversion values of 0.56 and 0.6 at 575°C, respectively, but were slowly deactivated at 600°C. This could be due to the interaction between the Ni particles and supports which could inhibit sintering at high temperatures as reported by Li *et al.*<sup>8</sup> It was observed that a trace of carbon monoxide was detected by the gas chromatograph when the Ni-CeO<sub>2</sub> catalyst was used at a reaction temperature of 600°C. This could be due to the redox properties of cerium ions ( $\text{Ce}^{3+} \leftrightarrow \text{Ce}^{4+}$ ), which was also observed from the TPR tests. In contrast, the Ni-Cu alloy catalyst exhibited lower methane conversion values of 0.05, 0.28 and 0.45, at 500, 550 and 575°C, respectively and slowly deactivated at 600°C with increasing reaction time, but abruptly deactivated completely in less than 30 min at 650°C. Ni-Cu alloys were extensively studied as catalysts for methane decomposition.<sup>18-23</sup> It has been widely accepted that the growth of carbon nanofibers by decomposition of hydrocarbons on Ni surface is based on adsorption-diffusion-precipitation mechanism. The hydrocarbon molecules first adsorb and dissociate on the Ni surface to form carbon atoms. The carbon species diffuse through the Ni particle and precipitate at the rear side of the nanoparticle to form carbon filaments.<sup>41, 42</sup> The step of dissociation and diffusion play a critical role and a balance between dissociation rate and diffusion rate has to be achieved to maintain a continuous growth of carbon-filaments. Copper itself is not active for methane dissociation but the presence of copper could significantly affect the electronic and surface properties of nickel. In lower reaction temperatures, the presence of copper atoms in the Ni-Cu alloy surface reduced the number of active sites, resulting in lower dissociation rates. In addition, the change of the electron density of the Ni unfilled d-band due to electron transfer from Cu to Ni atoms as indicated by the XPS results could also affect the activities of Ni atoms. Consequently, the Ni-Cu alloy catalyst exhibited lower methane conversion values as compared with those of the Ni catalyst at lower temperatures. At higher temperatures (> 550°C), the nickel catalyst deactivated rapidly due to the fact that the dissociation rate was faster than the diffusion rate, resulting in the encapsulation of the exposed nickel surfaces by the graphitic layers. Under this circumstance, the presence of copper atoms could modulate the dissociation rate as well as increase the diffusion rate due to the increase in the lattice parameter of Ni crystals as indicated by the XRD results. The balance

between dissociation and diffusion could be restored and subsequently the continuous growth of carbon-filaments occurred.

**3.3 Life span tests on the catalysts.** To study the life span of the catalyst, the reaction was carried out at a fixed temperature using pure methane until the complete deactivation of the catalyst (when methane conversion was less than 5%) and these methane conversion curves versus time for all the catalysts tested are shown in Figure 10. The Ni catalyst had a life span of 600 min while the Ni-Cu alloy, Ni-CeO<sub>2</sub> and Ni-TiO<sub>2</sub> catalysts exhibited life spans of 670, 790 and 840 min, respectively. The longer life spans of Ni-CeO<sub>2</sub> and Ni-TiO<sub>2</sub> catalysts were attributed to the smaller Ni particle sizes as well as the stabilizing effects of the supports. The Ni, Ni-CeO<sub>2</sub> and Ni-TiO<sub>2</sub> catalysts showed similar characteristics which involved three steps, *i.e.*, induction stage, plateau stage and deactivation stage.<sup>43</sup> In contrast, the methane conversion curve of the Ni-Cu alloy catalyst showed a wave plateau pattern for the initial 300 min, followed by a short plateau stage and a deactivation stage. This behaviour could be related to the changes in the atomic composition of the surface of Ni-Cu alloy particles during the reaction.<sup>42</sup> The carbon yield of the catalyst was theoretically calculated from the data in Figure 10 and was experimentally determined by the weight difference between the pristine catalyst and the deactivated catalyst. The experimental carbon yield values of the catalysts were very close to the theoretical values except for the Ni-CeO<sub>2</sub> catalyst as shown in Table 3. The significant difference for the Ni-CeO<sub>2</sub> catalyst could be due to the generation of carbon monoxide as detected by the gas chromatograph during the reaction. The Ni catalyst had a carbon yield of 121 g C per g of Ni at 550°C, which was lower than the value reported by Wang and Lua<sup>40</sup> The Ni-Cu alloy exhibited a carbon yield of 171 g C per g of Ni at 575°C, which was also less than the value of 250 g C per g of Ni as reported by Avdeeva *et al.*<sup>43</sup> These lower values obtained could be due to the large particle sizes and broad size distributions of Ni and Ni-Cu alloy particles in this study. The Ni-CeO<sub>2</sub> and Ni-TiO<sub>2</sub> catalysts achieved carbon yields of 204 and 256 g C per g of Ni at 575°C, respectively, which were higher than the value of 40% Ni/SiO<sub>2</sub> catalyst (estimated to be 170 g C per g of Ni at 575°C) as reported by Takenaka *et al.*<sup>9</sup> It should be noted that the carbon yields of all the catalysts tested could be improved by optimizing the reaction process such as the feed flow rate and catalyst mass.

**3.4 Carbon morphology.** Figure 11 shows the morphology of the used catalysts. The FESEM micrographs show that the resulting carbon materials for all the catalysts have a filamentous

structure. The diameters of the carbon filaments deposited on the Ni catalyst ranged from 20 to 100 nm. Comparing with the sizes of the pristine Ni particles, some carbon nanofibres with smaller diameters were observed, indicating the fragmentation of the Ni particles during the reaction. The elongated pear-shaped Ni particle (inset in Figure 11 (A)) with a long tail was located at the tip of the fibre, indicating tip growth mechanism of the fibre. When compared with the Ni catalyst, the carbon fibres obtained from the Ni-CeO<sub>2</sub> and Ni-TiO<sub>2</sub> catalysts exhibited more uniform diameters of 10-20 nm, which were very similar to the diameters of the Ni crystals in the supported catalysts. A closer inspection of the carbon filaments obtained from the Ni-TiO<sub>2</sub> catalyst exhibited thinner walls and larger hollow diameters than those of the carbon nanofibres obtained from the Ni-Ce catalyst as shown by the inserts in the TEM micrographs. In fact, the former carbon filaments were multiwalled-carbon nanotubes in nature while the latter were herring-bone nanofibres. The carbon obtained from the Ni-Cu alloy catalyst exhibited different morphology. The prominent feature of the carbon was the presence of branched carbon fibres, *i.e.*, octopus-like fibres, deposited on the multi-faceted Ni-Cu alloy particles as shown in Figure 11 (B). The formation of octopus-like fibres was surmised to be due to the segregation of copper atoms in the surface of the alloy catalyst which could result in additional faceted crystal planes for carbon growth.<sup>40</sup> This could be verified by the increase in methane conversion, resulting in a wave plateau in the methane conversion curve with time for the Ni-Cu catalyst as shown in Fig 10. Besides branched fibres, carbon filaments of a variety of diameters and lengths could also be observed. These results further indicated that the mechanism of carbon formation on the Ni-Cu catalyst was different from that on the Ni catalyst. The used catalysts were further characterized using XRD tests as shown in Figure 12. The nickel element in the catalysts was present in the metallic form without the formation of nickel carbide phase. The Ni-Cu alloy catalyst still exhibited its characteristic diffractions, indicating that the de-alloying process did not occur during the methane decomposition reaction. No distinct phase changes on the supports, *i.e.*, TiO<sub>2</sub> and CeO<sub>2</sub> phases, were observed after the methane decomposition reactions as compared with the XRD patterns of these phases in Fig. 7.

#### 4. CONCLUSION

Ni and Ni-Cu, Ni-TiO<sub>2</sub> and Ni-CeO<sub>2</sub> catalysts were synthesized by the sol-gel method using a branched surfactant Tween 20 as structure-directing agent in the first stage of preparation. EDX and XRD results indicated the presence of NiCl<sub>2</sub> in the metal oxides due to incomplete

hydrolysis of  $\text{Ni}^{2+}$  during the sol-gel process. After thoroughly washed,  $\text{NiCl}_2$  was removed and the resulting metal oxides and catalysts were fully characterized. The introduction of copper promoter and supports, *i.e.*,  $\text{TiO}_2$  and  $\text{CeO}_2$ , had significant effects on the structural properties and catalytic performance of the catalysts. The supported catalysts exhibited strong metal-support interactions as indicated by the TPR and XPS results which could enhance the stability and activity of the catalysts at higher temperatures than Ni catalyst. The presence of copper in the Ni-Cu catalyst as a promoter increased the working reaction temperature but decreased methane conversion values, indicating that the copper played a significant role in carbon nucleation and carbon diffusion during the carbon formation process. The Ni catalyst had a life span of 600 min at  $550^\circ\text{C}$ , resulting in a carbon yield of 121 g C/g Ni while the Ni-Cu, Ni- $\text{CeO}_2$  and Ni- $\text{TiO}_2$  catalysts had life spans of 670, 790 and 840 min at  $575^\circ\text{C}$ , resulting in carbon yields of 171, 204 and 256 g C/g Ni, respectively. Among the catalysts, the Ni- $\text{TiO}_2$  catalyst showed the best catalytic performance with a methane conversion of 45%, a life span of 840 min, and a carbon yield of 256 g C/g Ni at  $575^\circ\text{C}$ . It was found that the morphology of the resulting carbon deposits was dependent on the catalyst. With further optimization on the composition of the catalyst and the reaction conditions, Ni- $\text{TiO}_2$  catalyst provides a promising application for the production of hydrogen and carbon nanotubes by the TDM process.

## REFERENCES

1. N. Z. Muradov, T. N. Veziroglu, *Int. J. Hydrogen Energy*, 2008, **33**, 6804-6839
2. M. Balat, *Int. J. Hydrogen Energy*, 2008, **33**, 4013-4029
3. H. F. Abbas, W.M.A. W. Daud, *Int. J. Hydrogen Energy*, 2010, **35**, 1160-190
4. J. Dufour, D. P. Serrano, *Int. J. Hydrogen Energy*, 2009, **34**, 1370-1376
5. Y. D. Li, D. X. Li, G. W. Wang, *Catal. Today*, 2011, **162**, 1-48
6. R. M. Navarro, M. A. Pena, *Chem. Rev.*, 2007, **107**, 3952-3991
7. Y. Zhang, K. J. Smith, *Catal. Lett.*, 2004, **95**, 7-12.
8. Y. D. Li, J. L. Chen, Y. N. Qin, L. Chang, *Energy & Fuel*, 2000, **14**, 1188-1194
9. S. Takenaka, S. Kobayashi, H. Ogihara, K. Otsuka, *J. Catal.*, 2003, **217**, 79-87
10. S. Takenaka, E. Kato, Y. Tomikubo, K. Otsuka, *J. Catal.*, 2003, **219**, 176-185
11. M. A. Ermakova, D. Y. Ermakov; G. G. Kuvshinov, L. M. Plyasova, *J. Catal.*, 1999, **187**, 77-84
12. M. J. Lazaro, Y. Echegoyen, I. Suelves, J. M. Palacios, R. Moliner, *Appl. Catal. A: Gen.*, 2007, **329**, 22-29
13. Y. Echegoyen, I. Suelves, M. J. Lazaro, M. L. Sanjuan, R. Moliner, *Appl. Catal. A: Gen.*, 2007, **333**, 229-237
14. H. Y. Wang, R. T. K. Baker, *J. Phys. Chem. B*, 2004, **108**, 20273-20277
15. Y. Li, B. C. Zhang, X. L. Tang, Y. D. Xu, W. J. Shen, *Catal. Commun.*, 2006, **7**, 380-386.
16. I. Suelves, M. J. Lazaro, R. Moliner, Y. Echegoyen, J. M. Palacios, *Catal. Today*, 2006, **116**, 271-280.
17. P. Wang, E. Tanabe, K. Ito, J. Jia, H. Morioka, T. Shishido, K. Takehira, *Appl. Catal. A: Gen.*, 2002, **231**, 35-44.
18. D. X. Li, J. L. Chen, Y. D. Li, *Int. J. Hydrogen Energy*, 2009, **34**, 299-307
19. T. V. Reshetenko, L. B. Avdeeva, Z. R. Ismagilov, A. L. Chuvilin, V. A. Ushakov, *Appl. Catal. A: Gen.*, 2003, **247**, 51-63.
20. L. Dussau, J. C. Dupin, C. Guimon, M. Monthieux, N. Latorre, T. Ubieta, E. Romeo, C. Royo, A. Monzon, *J. Catal.*, 2007, **251**, 223-232
21. A. R. Naghash, Z. Xu, T. H. Etsell, *Chem. Mater.* 2005, **17**, 815-821.

22. A. Hornés, P. Beraa, M. Fernández-García, A. Guerrero-Ruiz, A. Martínez-Arias, *Appl. Catal. B: Environ.*, 2012, **111-112**, 96-105
23. J. L. Pinilla, I. Suelves, M. J. Lazaro, R. Moliner, J. M. Palacios, *Int. J. Hydrogen Energy*, 2008, **33**, 2515-2524.
24. M. J. Lazaro, Y. Echevoyen, C. Alegre, I. Suelves, R. Moliner, J. M. Palacios, *Int. J. Hydrogen Energy*, 2008, **33**, 3320-3329.
25. I. Suelves, J. L. Pinilla, M. J. Lazaro, R. Moliner, J. M. Palacios, *J. Power Sources*, 2009, **192**, 35-42.
26. J. L. Pinilla, R. Moliner, I. Suelves, M. J. Lazaro, Y. Echevoyen, J. M. Palacios, *Int. J. Hydrogen Energy*, 2007, **32**, 4821-4829.
27. D. P. Debecker, P. H. Mutin, *Chem. Soc. Rev.*, 2012, **41**, 3624-3650
28. D. A. Ward, E. I. Ko, *Ind. Eng. Chem. Res.*, 1995, **34**, 421-433
29. L. Y. Piao, Y. D. Li, J. L. Chen, L. Chang, J. Y. Lin, *Catal. Today*, 2002, **74**, 145-155.
30. R. Takahashi, S. Sato, T. Sodesawa, M. Yabuki, *J. Catal.*, 2001, **200**, 197-202
31. J. Fan, S. W. Boettcher, G. D. Stucky, *Chem. Mater.*, 2006, **18**, 6391-6396
32. L. F. Liotta, G. D. Carlo, G. Pantaleo, G. Deganello, *Appl. Catal. B: Environ.*, 2007, **70**, 314-322
33. Y. Shen, A. C. Lua, *Sci. Rep.*, 2013, **3**, 3037
34. A. C. Lua, H. Y. Wang, *Appl. Catal. B: Environ.*, 2013, **132-133**, 469-478
35. A. F. Baes, R. E. Mesmer, *The Hydrolysis of Cations*, Wiley-Interscience, New York, 1976; and J. Burgess, *Metal Ions in Solution*, Ellis Horwood, Chichester, England, 1978
36. Z. X. Cheng, X. G. Zhao, J. L. Li, Q. M. Zhu, *Appl. Catal. A: Gen.*, 2001, **205**, 31-36
37. S. Damyanova, J. M. C. Bueno, *Appl. Catal. A: Gen.*, 2003, **253**, 135-150
38. A. R. Naghash, T. H. Etsell, S. Xu, *Chem. Mater.*, 2006, **18**, 2480-2488
39. K. W. Park, J. H. Chio, B. K. Kwon, S. A. Lee, Y. E. Sung, H. Y. Ha, S. A. Hong, H. S. Kim, A. Wieckowski, *J. Phys. Chem. B*, 2002, **106**, 1869-1877
40. H. Y. Wang, A. C. Lua, *J. Phys. Chem. C*, 2012, **116**, 26765-26775
41. R. T. K. Baker, *Carbon*, 1989, **27**, 315-323

42. N. M. Rodriguez, M. S. Kim, R. T. K. Baker, *J. Catal.*, 1993, **140**, 16-29
43. L. B. Avdeeva, O. V. Goncharova, D. I. Kochubey, V. I. Zaikovskii, L. M. Plyasova, B. N. Novgorodov, S. K. Shaikhutdinov, *Appl. Catal. A: Gen.*, 1996, **141**, 117-129

## Tables

Table 1 Atomic composition, BET surface areas and pore sizes of the metal oxides

Sample	Elemental composition (mmol.%) <sup>a</sup>	BET surface area (m <sup>2</sup> /g)	Pore size (Å) <sup>b</sup>
NiO	Ni(47.8):O(48.5):Cl(3.7) <sup>*</sup>	66	36
	Ni (47.2):O(52.8) <sup>**</sup>		
NiO-TiO <sub>2</sub>	Ni(15.4):Ti(16.3):O(64.4):Cl(3.9) <sup>*</sup>	161	90
	Ni(13.7):Ti(18.9):O(67.4) <sup>**</sup>		
NiO-CeO <sub>2</sub>	Ni(14.5):Ce(15.7):O(60.8):Cl(9) <sup>*</sup>	133	98
	Ni(8.7):Ce(20.9):O(70.4) <sup>**</sup>		
NiO-CuO	Ni(20.3):Cu(24.4):O(52.7):Cl(2.6) <sup>*</sup>	13	37
	Ni(21.4):Cu(25.6):O(53) <sup>**</sup>		

<sup>a</sup> Determined from EDX tests. For each sample, five tests were carried out and the average values are given.

<sup>b</sup> Determined by  $4V/A$ , where V and A are the pore volume and BET surface area, respectively.

<sup>\*</sup> Results for the samples before wash.

<sup>\*\*</sup> Results for the samples after thorough wash.

Table 2 Binding energies of Ni 2p<sub>3/2</sub> obtained from curve-fitted values of experimental XPS spectra, crystal sizes obtained from XRD patterns and reduction temperatures determined by TPR.

Sample	Ni 2p <sub>3/2</sub> (eV) <sup>a</sup>				Crystal size (nm) <sup>b</sup>		RT (°C) <sup>c</sup>
	Ni(I)	Ni(II)	Ni(III)	Satellite	Before reduction	After reduction	
Ni	852.1	854.9	856.5	861.3	36	24	377
Ni-Cu	851.6	854.3	857.8	861.9	26	30	235, 340
Ni-TiO <sub>2</sub>	852.7	855.4	855.9	861.5	20	14	409
Ni-CeO <sub>2</sub>	852.8	855.6	857.1	862.1	21	18	418

<sup>a</sup> Estimated experimental error: ± 0.1 eV.

<sup>b</sup> Determined from XRD patterns based on Scherrer equation.

<sup>c</sup> RT= reduction temperature as determined from the TPR tests.

Table 3 Methane conversion and carbon yield of the catalyst. For the Ni catalyst, the decomposition reaction was carried out at 550°C while for the Ni-Cu, Ni-TiO<sub>2</sub> and Ni-CeO<sub>2</sub> catalysts, the reactions were carried out at 575°C to determine the carbon yield values.

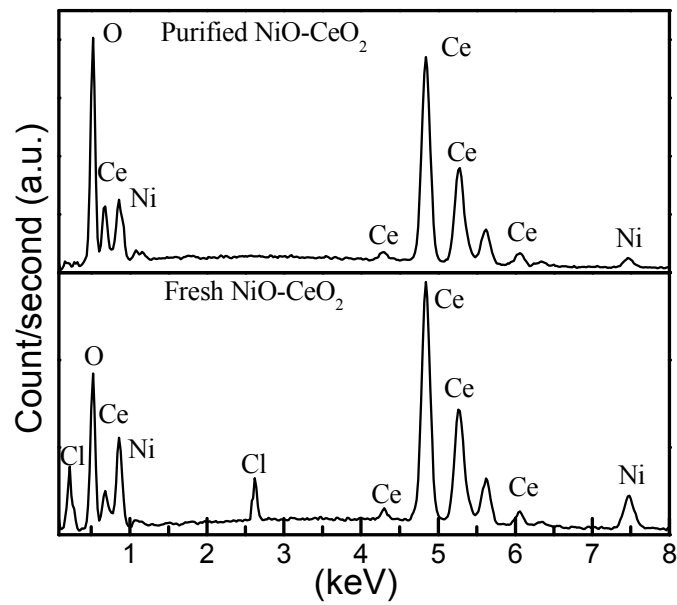
Sample	Methane conversion				Carbon yield (g C/g Ni) <sup>a</sup>	Carbon yield (g C/g Ni) <sup>b</sup>
	500°C	550°C	575°C	600°C		
Ni	0.25	0.39	0.46*		123	121
Ni-Cu	0.05	0.28	0.45	0.62*	174	171
Ni-TiO <sub>2</sub>	0.28	0.47	0.56	0.66*	259	256
Ni-CeO <sub>2</sub>	0.30	0.47	0.60	0.71*	227	204

\* Unstable methane conversion under the respective reaction temperatures.

<sup>a</sup> Theoretical carbon yield value calculated by integration.

<sup>b</sup> Carbon yield value determined by measuring the sample before and after the reaction.

## Figures

Figure 1 EDX curves of NiO-CeO<sub>2</sub> before and after wash

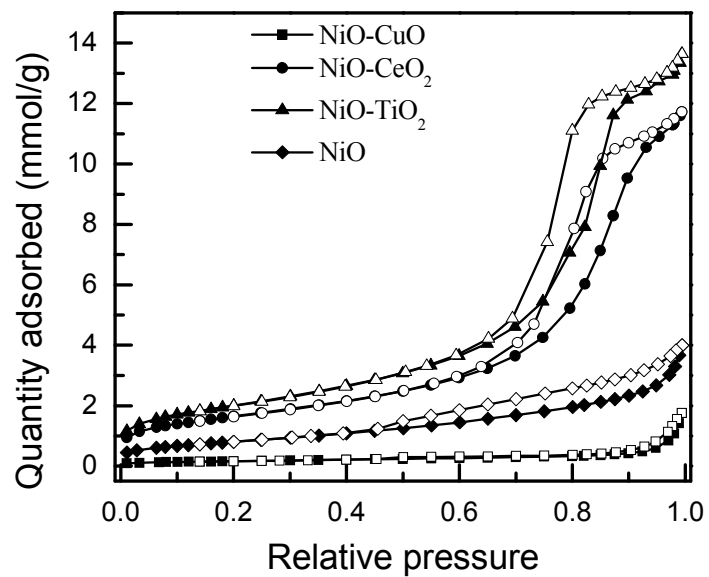


Figure 2 N<sub>2</sub> adsorption-desorption isotherms of the metal oxides

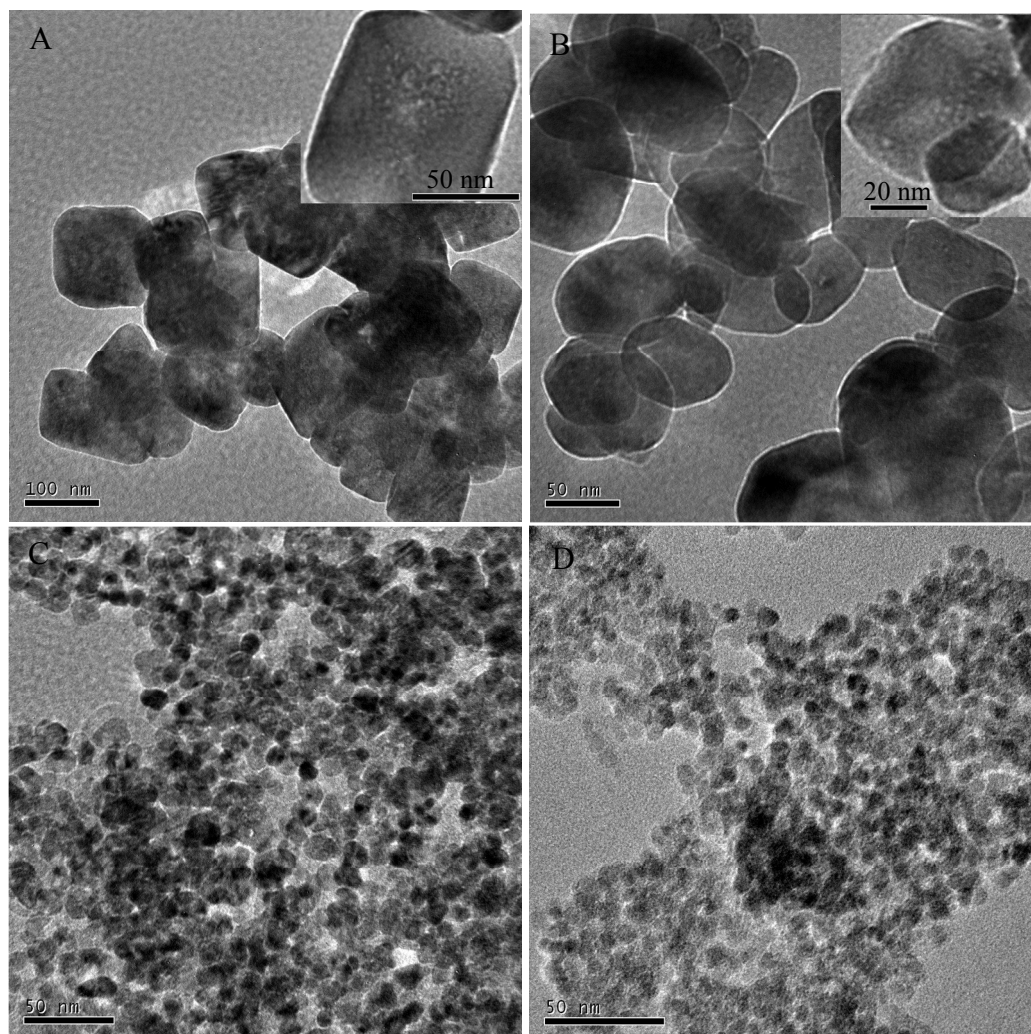


Figure 3 TEM micrographs of (A) NiO, (B) NiO-CuO, (C) NiO-CeO<sub>2</sub> and (D) NiO-TiO<sub>2</sub>

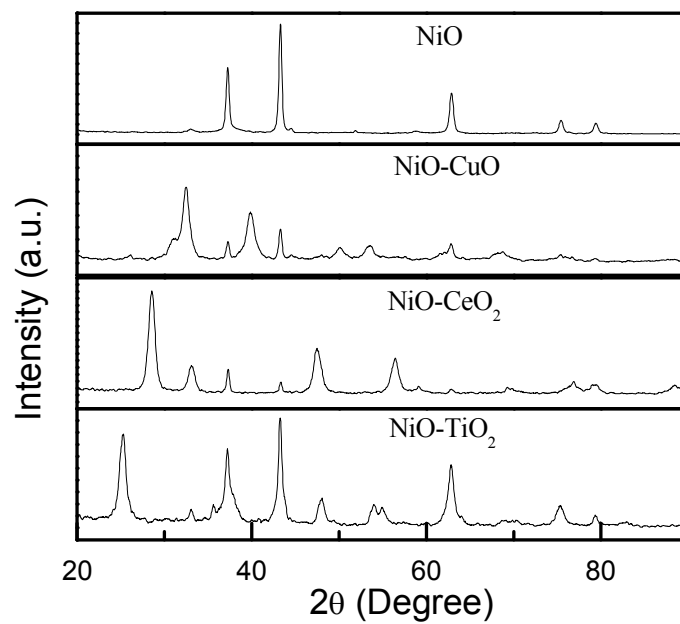


Figure 4 XRD patterns of the metal oxides before hydrogen reduction

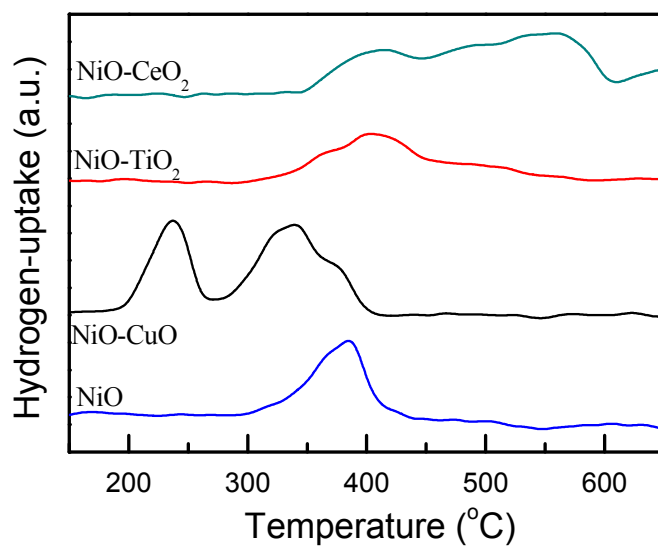


Figure 5 Temperature-programmed reduction curves of the metal oxides

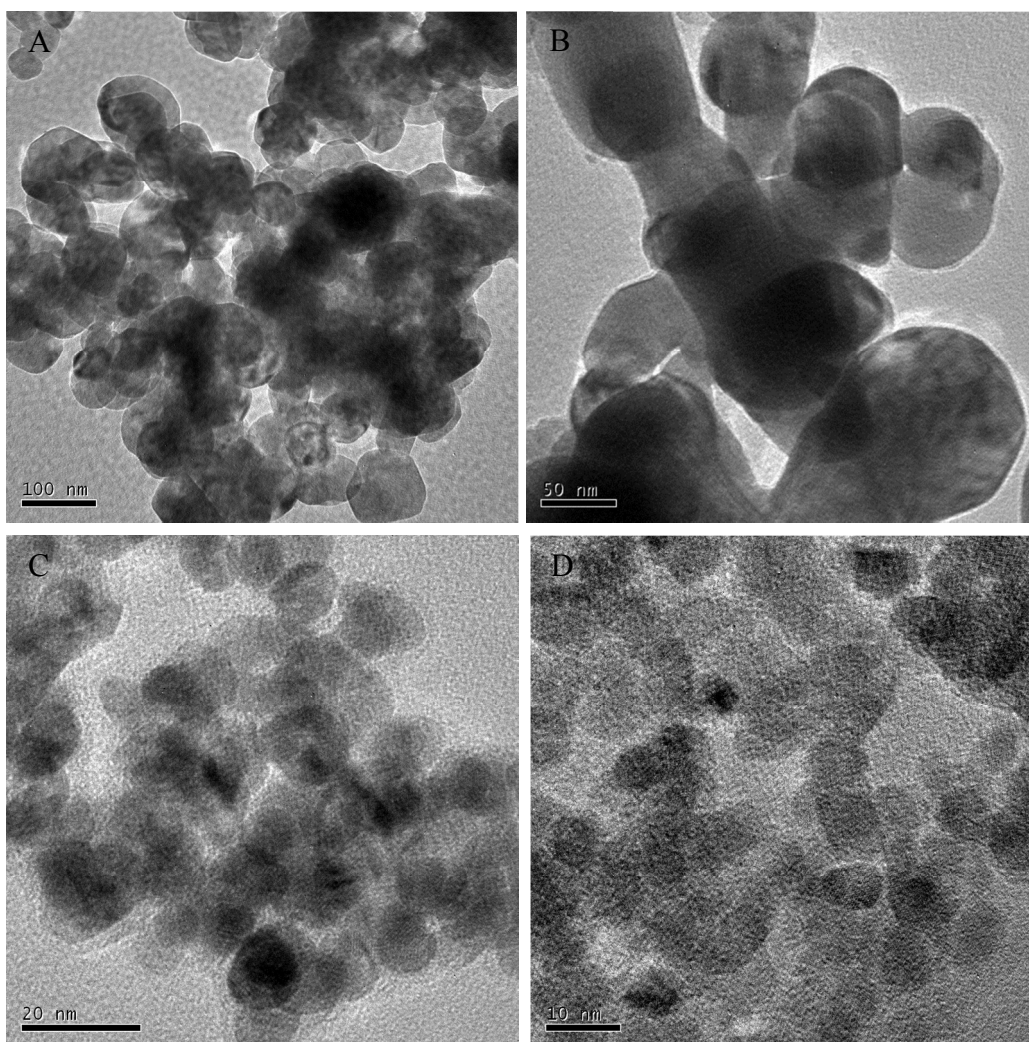


Figure 6 TEM micrographs of (A) Ni, (B) Ni-Cu, (C) Ni-CeO<sub>2</sub> and (D) Ni-TiO<sub>2</sub>

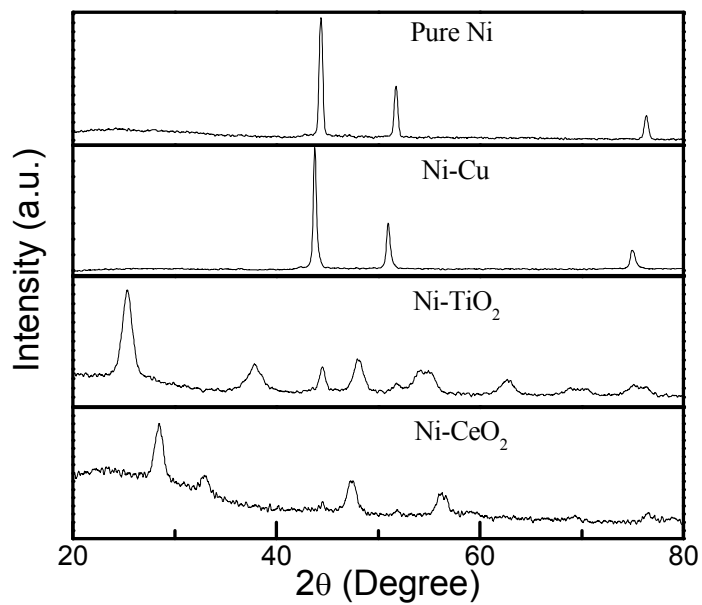


Figure 7 XRD patterns of the catalysts after hydrogen reduction

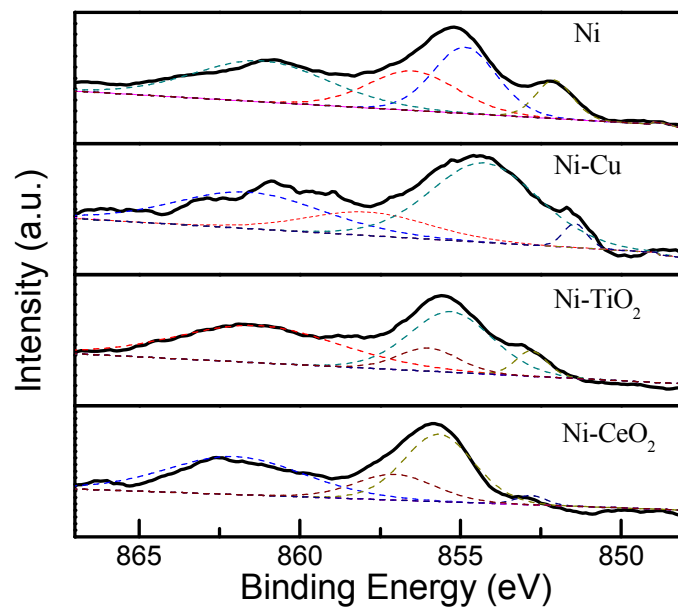


Figure 8 X-ray photoelectron spectra of Ni 2p<sub>3/2</sub> of the catalysts after hydrogen reduction

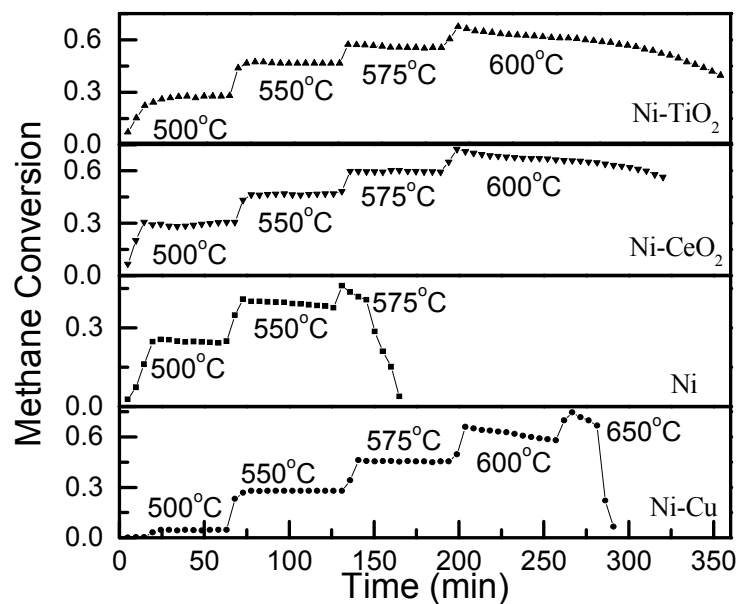


Figure 9 Methane conversion over the catalysts at stepwise heating temperatures (10 mg of metallic nickel was used for all the catalyst samples,  $\text{CH}_4:\text{N}_2 = 3:5$ , total flow rate =  $20 \text{ mL}\cdot\text{min}^{-1}$ , weight hour space velocity was around  $45 \text{ L CH}_4\cdot\text{h}^{-1}\cdot\text{g}^{-1}_{\text{Ni}}$ ).

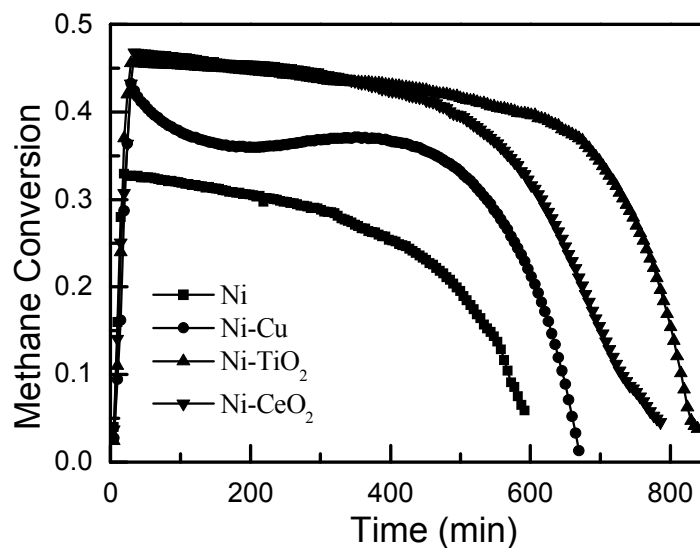


Figure 10 Methane conversion curves versus time until complete catalyst deactivation (5 mg of metallic nickel was used for all the catalyst samples, pure methane, volume flow rate of methane =  $7.5 \text{ mL} \cdot \text{min}^{-1}$ , weight hour space velocity was around  $90 \text{ L CH}_4 \cdot \text{h}^{-1} \cdot \text{g}^{-1}_{\text{Ni}}$ ). For the Ni sample, the reaction was carried out at  $550^\circ\text{C}$  while for the Ni-Cu, Ni-TiO<sub>2</sub> and Ni-CeO<sub>2</sub> samples, the reactions were carried out at  $575^\circ\text{C}$ .

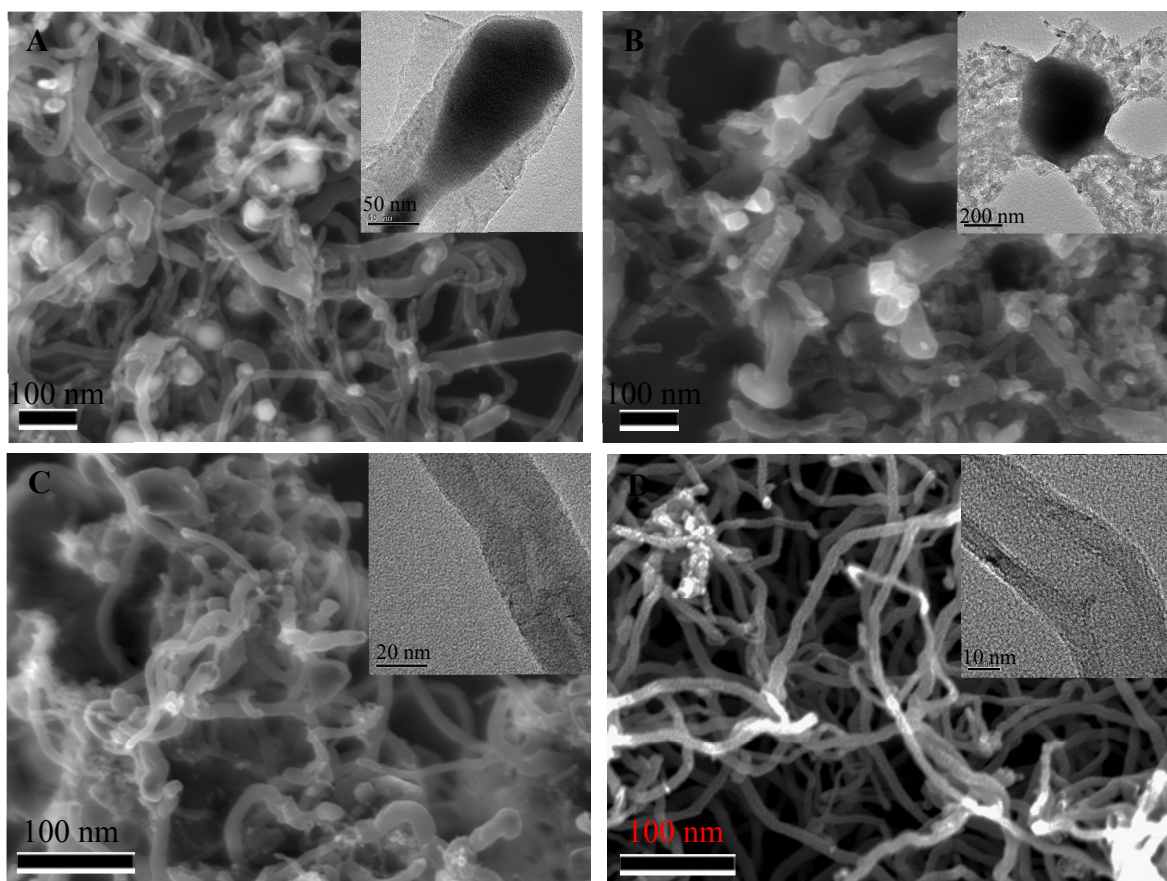


Figure 11 FESEM micrographs of the used catalysts (A) Ni, (B) Ni-Cu, (C) Ni-CeO<sub>2</sub> and (D) Ni-TiO<sub>2</sub>

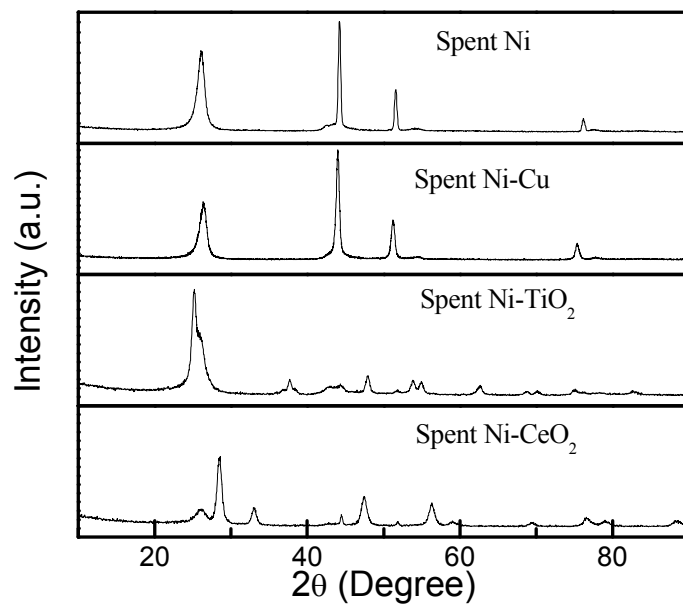


Figure 12 XRD patterns of the used catalysts